ADVANCED FUNCTIONAL MATERIALS
www.afm-journal.de

High-Performance Neutral-Color Semitransparent Organic Photovoltaics with Optical and Thermal Management

*Jiangsheng Yu, Xin Liu, Jie Zhou, and Gang Li**

Neutral-color semitransparent organic photovoltaics (ST-OPVs) offer potential opportunities to improve solar energy harvesting in integrated buildings. Here, high-performance multifunctional neutral-color ST-OPVs are successfully fabricated by integrating a Ag/TeO_2/Ag/TeO_2-based Fabry–Perot resonant optical coating (FPOC). Two coupled resonators of FPOCs are successfully fabricated to manipulate two adjacent transmission peaks in the visible region (380–780 nm) and high reflection from 1200 to 2500 nm, revealing its excellent color rendering index (CRI) tunability and thermal insulation. The 75 nm FPOC-integrated ST-OPV exhibits a CRI of 97.31, a high average visible transmittance of 43.15%, and a light utilization efficiency of 3.90% with superior thermal insulation properties, where the highest total and near-infrared solar-energy-rejected dual functional efficiencies are 2.92% and 3.47%, respectively. The record CRI value of 99.23 is achieved for the 65 nm FPOC-integrated ST-OPVs. Attributed to the angular tolerance of FPOC, the neutral-color ST-OPVs exhibit good angular insensitivity up to ±60°. The results demonstrate the flexibility and multifunctionality of visible dual-band-pass Ag/TeO_2/Ag/TeO_2-based FPOC for constructing neutral-color, heat-insulated, and angular-insensitive ST-OPVs, opening up a new avenue for the realization of smart power windows.

1. Introduction

Organic photovoltaics (OPVs) have emerged as an innovative contender in the field of sustainable energy technologies due to their numerous features, such as low production cost, semi-transparency, mechanical flexibility, solution preparation, and lightweight.[1–6] With the rapid development of functional-conjugated materials and device engineering, the power conversion efficiency (PCE) of single-junction OPV devices has been reaching 20%.[7–10] The emerging nonfullerene acceptors are currently the major focus of research for OPVs, where Y6 derivatives are the most representative ones.[11] For numerous Y6-derivative-based OPVs with PCE exceeding 19%, the photoactive layer exhibits a discrete absorption extending to the near-infrared (NIR) region with a bandgap of about 1.3 eV.[12–16] It is beneficial for constructing high-performing semitransparent organic photovoltaics (ST-OPVs), which aim at maximizing both PCE and average visible transmittance. ST-OPVs have attracted great interest in the scientific and industrial communities due to their many promising applications in building-integrated photovoltaics (BIPVs), including smart windows, vehicle skylights, greenhouse rooftops, and large public spaces.[17–22]

The development of near-infrared photoactive materials, transparent electrode engineering, and optical management structures are the main strategies for efficient ST-OPVs.[23–26] ST-OPVs based on Y6 derivatives can achieve ≈80% of the PCE of opaque devices with an average visible transmittance (AVT) of nearly 20%.[27] Highly efficient and reproducible ST-OPVs have been fabricated with ultrathin metal films as transparent electrodes, such as gold (Au) and silver (Ag) with a thickness of about 10–20 nm.[28–31] An ideal transparent photovoltaic device for BIPV applications should have several characteristics,[32] including high light utilization

J. Yu, G. Li
Department of Electrical and Electronic Engineering
Research Institute for Smart Energy (RISE)
Photonic Research Institute (PRI)
The Hong Kong Polytechnic University
Hong Kong 999077, China
E-mail: gang.w.li@polyu.edu.hk

The ORCID identification number(s) for the author(s) of this article can be found under https://doi.org/10.1002/adfm.202406070

J. Yu, X. Liu
School of Electronic and Optical Engineering
Nanjing University of Science and Technology
Nanjing 210094, China

J. Zhou
School of Chemistry and Chemical Engineering
Nanjing University of Science and Technology
Nanjing 210094, China

DOI: 10.1002/adfm.202406070

efficiency (LUE),[33–35] high AVT,[36,37] the color rendering index (CRI)[38] approaching 100 for displaying the intrinsic color of the object, and superior lifespan.[39] As early as 2012, Chen et al. demonstrated the suitability of the poly[[4,8-bis[5-(2-ethylhexyl)-2-thienyl]benzo[1,2-b:4,5-b′]dithiophene-2,6-diyl][2-(2-ethyl-1-oxohexyl)thieno[3,4-b]thiophenediyl]]:[6,6]-phenyl-C71-butyric acid methyl ester (PBDTTT-C-T:$PC_{71}BM$) active layer system for power generation window applications, exhibiting an impressive transparency color rendering capability with a CRI of 96 and PCE of 6%.[40] By integrating 1D photonic crystals (1DPCs) into the transparent electrodes, a further increase in CRI approaching 100 was achieved for fullerene-based ST-OPVs.[41,42] Considering the rapid progress of landmark Y6-derivative-based OPVs, ST-OPVs further step challenges to balance the metrics among CRI, AVT, PCE, and LUE. For example, Yuan et al. used NIR-acceptor-based ST-OPVs (iridium-based polymer (PM6-Ir1):2,2′-((2Z,2′Z)-((12,13-bis(2-butyloctyl)-3,9-dinonyl-12,13-dihydro-[1,2,5]thiadiazolo[3,4-e]thieno[2″,3″:4′,5′]thieno[2′,3′:4,5]pyrrolo[3,2-g]thieno[2′,3′:4,5]thieno[3,2-b]indole-2,10-diyl)bis(methaneylylidene))bis(5,6-dichloro-3-oxo-2,3-dihydro-1H-indene-2,1-diylidene))dimalononitrile (BTP-eC9):$PC_{71}BM$) and 1DPCs to achieve a trade-off between device performance and neutral color, where a high CRI of 96.5 is reported, but the LUE is only 2.09% with a low AVT of 20%.[43] In our own work, we demonstrated a 5.35% record LUE by an aperiodic band-pass electrode to almost fully release the NIR potential, with high PCE and LUE in a broad range. However, for many-layers optical thin film structure, the angular dependence performance is an unescapable effect,[44,45] and the CRI values are below 90.[33] Fabry–Perot (FP) resonant cavity structure[46] is also an effective way to manage optical properties for ST-OPVs. Metal–optical-dielectric-layer–metal-based microcavity[47] is utilized to construct cyan color ST-OPV with a CRI of 92.5, and serves as a visible color filter that can possess a high reflectivity in the NIR region.[48,49] While traditional FP resonant cavity has potential for actualizing high-performance neutral-color ST-OPVs by optical and thermal management, its narrow-band feature is not enough to cover the whole visible region (380–780 nm), leaving challenges for power generation windows.

To achieve a neutral color with a CRI value approaching 100, the absorption distribution in the visible region should be flat. Herein, two coupled resonators for FP resonant optical coatings (FPOCs) are designed to manipulate two adjacent transmission peaks in the visible region and high reflection from 1200 to 2500 nm, implying its excellent CRI tunability and thermal insulation. We first fabricated conventional ST-OPVs with PM6 (poly((4,8-bis(5-(2-ethylhexyl)-4-fluoro-2-thienyl)benzo[1,2-b:4,5-b′]dithiophene-2,6-diyl)-2,5-thiophenediyl(5,7-bis(2-ethylhexyl)-4,8-dioxo-4H,8H-benzo[1,2-c:4,5-c′]dithiophene-1,3-diyl)-2,5-thiophenediyl)): BTP-eC9:L8-BO (2,2′-((2Z,2′Z)-((3,9-bis(2-butyloctyl)-12,13-bis(2-ethylhexyl)-12,13-dihydro-[1,2,5]thiadiazolo[3,4-e]thieno[2″,3″:4′,5′]thieno[2′,3′:4,5]pyrrolo[3,2-g]thieno[2′,3′:4,5]thieno[3,2-b]indole-2,10-diyl)bis(methaneylylidene))bis(5,6-difluoro-3-oxo-2,3-dihydro-1H-indene-2,1-diylidene))dimalononitrile) as active layer and Au/Ag hybrid transparent electrode, achieving a decent LUE of 3.82% with a PCE of 9.81%, AVT of 38.99%, and CRI of 81.21. We noted a transmission peak at 400–500 nm and a transmission valley at 500–700 nm with different amplitudes occurring in the absorption distribution of the active layer. The optical properties of Ag/TeO_2/Ag/TeO_2-based FPOCs were systematically investigated through optical simulations and experimental preparation. The results indicated that Ag/TeO_2/Ag/TeO_2-based FPOCs can be designed as color modulation of ST-OPVs and visible band-pass filters with excellent thermal insulation. FPOC-integrated ST-OPVs were fabricated with the architecture of antireflection coating (ARC)/indium tin oxide (ITO)/poly(3,4-ethylenedioxythiophene) polystyrene sulfonate (PEDOT:PSS)/PM6:BTP-eC9:L8-BO (0.8:1:0.2)/aliphatic amine-functionalized perylene-diimide (PDINN)/Au(0.8 nm)/Ag (7 nm)/TeO_2/Ag (17 nm)/TeO_2. The highest LUE of 3.90% can be achieved in derived devices with a 75 nm active layer, with a distinguished CRI of 97.31, and an AVT of 43.15%. Meanwhile, the 75 nm FPOC-integrated ST-OPV exhibits a total solar energy rejection (T-SER) of 75% and NIR solar energy rejection (NIR-SER) of 89.11%, ultimately leading to a high-performance total solar energy rejection dual-function efficiency (T-DFE) of 2.92% and NIR solar energy rejection dual-function efficiency (NIR-DFE) of 3.47%, which realized 20% enhancement compared to the counterpart device. The highest CRI value of 99.23 is recorded for the 65 nm FPOC-integrated devices. Impressively, attributed to the angular tolerance of FPOC, the neutral-color ST-OPVs exhibit good angular insensitivity up to ±60°, which keeps the CRI value almost constant—an important feature for visual applications. The visible dual-band-pass Ag/TeO_2/Ag/TeO_2-based FPOCs can be utilized for the realization of efficient neutral-color ST-OPVs with color rendering properties approaching 100, a high AVT of over 45%, a superior solar energy rejection, and angular insensitivity. This breakthrough demonstrates the enormous potential of ST-OPVs as a viable and promising green energy solution for a more sustainable future.

2. Results and Discussion

The photovoltaic performance of ST-OPVs is mainly affected by active layer material and transparent electrodes. Herein, a ternary active layer, namely PM6:BTP-eC9:L8-BO (Figure S1, Supporting Information) with a relatively low donor ratio of 0.8:1:0.2 was used to explore the balance between PCE and AVT of ST-OPVs.[33] Bare thin Ag film below 10 nm has inferior optical and electrical properties due to the strong surface plasmon resonance effect of isolated Ag islands. Ultrathin Au as the seed layer for the transparent electrode can be utilized to improve the transmittance and photovoltaic performance of ST-OPVs, simultaneously. The 0.8/7 nm Au/Ag film presented a slightly higher transmittance and reduced resistance by an order of magnitude compared to the bare 7 nm Ag film (Figure S2, Supporting Information). To investigate the effect of 0.8 nm Au as the seed layer, the photovoltaic performance of ST-OPVs was explored with an architecture of ITO/ PEDOT:PSS/PM6:BTP-eC9:L8-BO (0.8:1:0.2, 110 nm)/PDINN/Au/Ag. As a result, ST-OPVs with Au/Ag hybrid transparent electrode exhibited a high LUE of 3.50% along with enhanced short-circuit current density (J_{SC}) of 17.57 mA cm^{-2}, open-circuit voltage (V_{OC}) of 0.853 V, fill factor (FF) of 76.52%, PCE of 11.47%, and AVT of 30.52%, which is streets ahead of the counterpart one with a LUE of 2.86%, as listed in

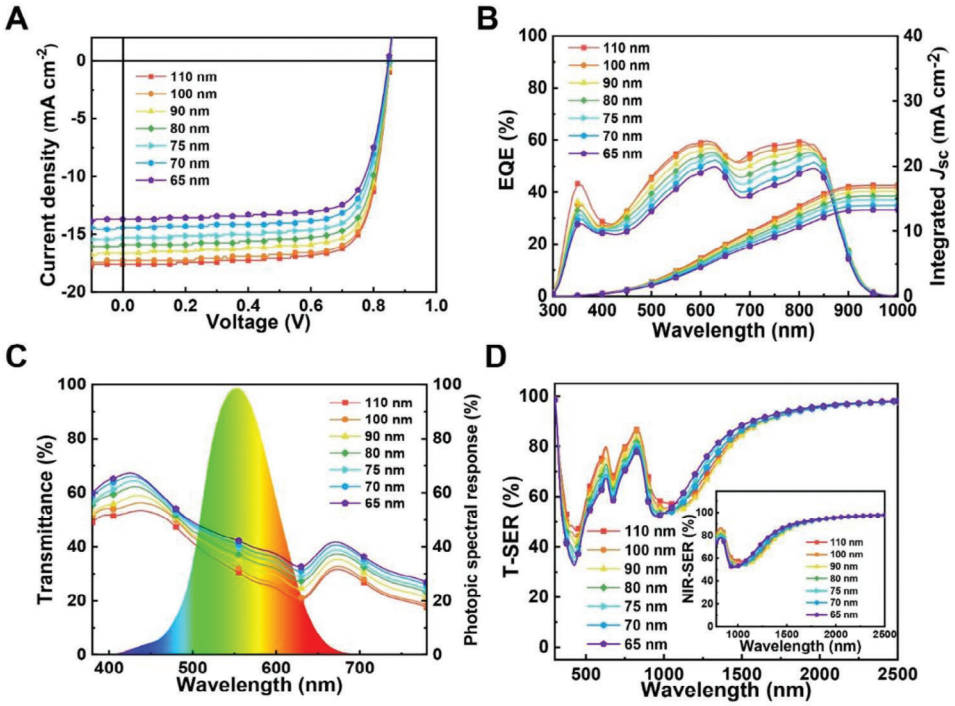

Figure 1. Photovoltaic performance and optical properties of the Au/Ag ST-OPVs (65–110 nm). A) *J–V* curves. B) EQE curves. C) Transmittance spectra (380–780 nm). D) T-SER spectra (300–2500 nm), and NIR-SER spectra (780–2500 nm).

Table S1 (Supporting Information). To further reveal the photovoltaic performance of ST-OPVs, different thicknesses of the active layer were fabricated between 65 to 110 nm. The relative *J–V* curves, external quantum efficiency (EQE) curves, and transmittance spectra (380–780 nm) for devices are shown in **Figure** 1A–C. With the decreasing thickness from 110 to 65 nm, the J_{SCs} of ST-OPVs were sequentially decreased from 17.57 to 13.69 mA cm^{-2}, while the AVT values were gradually increased from 30.52% to 41.78% (Table S2, Supporting Information). The V_{OC} and FF values exhibited negligible experimental fluctuations at 0.85 V and 75%. Consequently, a champion LUE of 3.82% was achieved for 75 nm ST-OPVs, along with a PCE of 9.81%, an AVT of 38.91%, and a CRI of 81.21. It is worth noting that the transmittance curves of devices were not increased uniformly with the decreasing thickness of the active layer, which is attributed to the interference effect of multilayer films. Further decreasing the active layer's thickness will not increase the CRI of device (Table S2, Supporting Information).

The thermal insulation performance of ST-OPVs was also investigated. The T-SER (λ = 300–2500 nm) and NIR-SER (λ = 780–2500 nm)[50] were measured, as shown in Figure 1D. The T-SER values were reduced from 71.23% to 66.05% with the decreasing active layer's thickness, while the NIR-SER values remained at around 75% (Table S2, Supporting Information). Considering the dual function of ST-OPV with power generation and thermal insulation capabilities,[49–51] herein, we define the T-DFE and the NIR-DFE of ST-OPVs as follows

$$\text{T-DFE} = \text{LUE} \times \text{T-SER} \quad (1)$$

$$\text{NIR-DFE} = \text{LUE} \times \text{NIR-SER} \quad (2)$$

The highest T-DFE and NIR-DFE values were 2.57% and 2.89% for 75 nm ST-OPVs, respectively. The Commission Internationale de l'Éclairage (CIE) 1931 coordinates (x, y) are one key factor in evaluating the optical performance of ST-OPVs. Compared to the AM1.5G coordinates (0.3202, 0.3324), the CIE 1931 coordinates of the ST-OPVs were shifted from (0.2687, 0.2876) to (0.2898, 0.3017) with the decreasing thickness of active layer (65–110 nm, Table S2 and Figure S3, Supporting Information). The variation tendencies of electrical and optical parameters for ST-OPVs were further verified by an optical simulation with the transfer matrix method. The complex refractive indexes[31] of each composite layer ($\tilde{n}(\lambda) = n(\lambda) + ik(\lambda)$) were measured by spectroscopic ellipsometry, as listed in Figure S4 (Supporting Information). The AVT values of the experimental and simulated ST-OPVs were almost consistent (Figure S5A, Supporting Information). Herein, the simulated internal quantum efficiency (IQE) is assumed at 100%. The simulated J_{SC} values of ST-OPVs also exhibited a similar trend compared with the experimental ones, as shown in Figure S5B (Supporting Information). As shown in Figure S6 (Supporting Information), the relationship between the LUE and the active layer's thickness (0–200 nm) and Ag (7–20 nm) was further simulated, with the assumptions of an open-circuit voltage at 0.855 V and a FF value of 80%. The results showed that the LUE value declined as the thickness of Ag increased, reaching a maximum value of 4% when the active layer's thickness was at 60–70 nm.

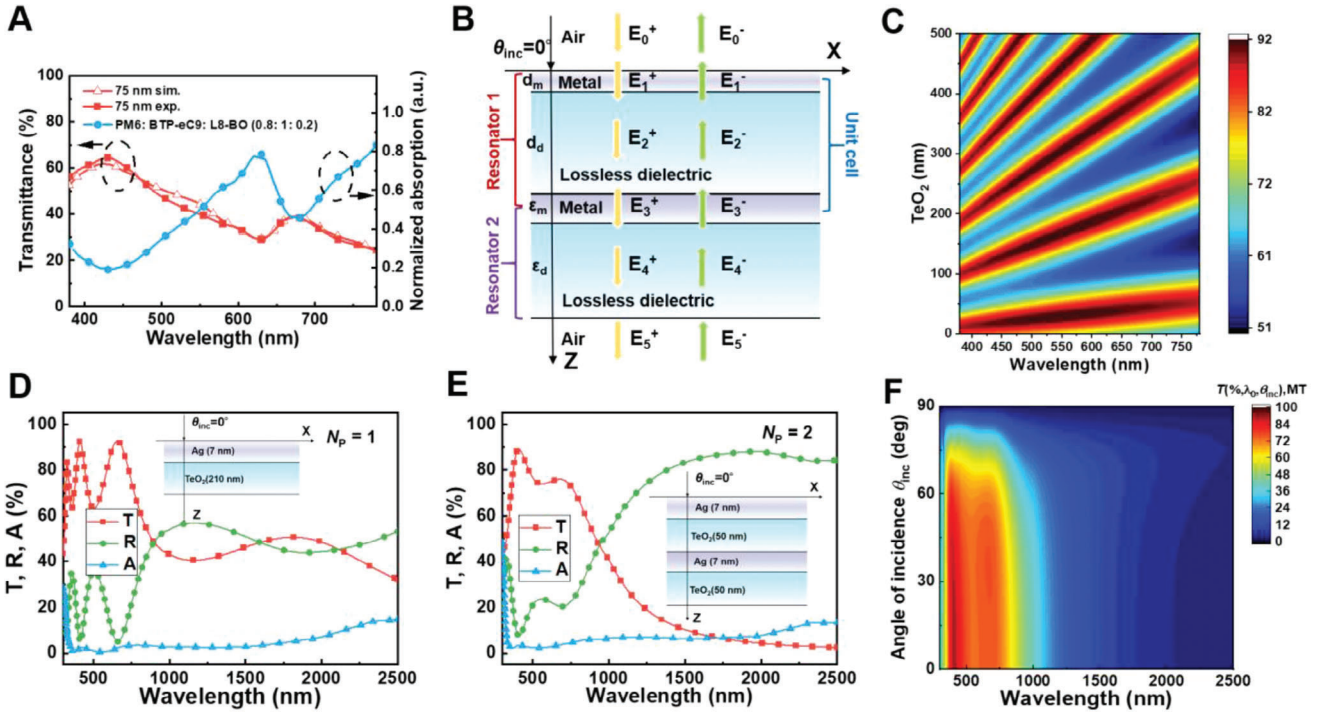

Figure 2. Fabry–Perot resonant optical coatings. A) The experimental and simulated transmittance spectra (380–780 nm) and normalized absorption curve of PM6:BTP-eC9:L8-BO (0.8:1:0.2) active layer. B) The schematic diagram of the multilayer stacking FPOC structure, where d_m and d_d represent the thicknesses of the metal and dielectric layers, respectively, ϵ_m and ϵ_d are the dielectric constants, N_p is the number of periods in the cell, and θ_{inc} is the angle of incidence. C) The simulated transmittance spectra of Ag (7 nm)/TeO_2 (0–500 nm). D) Simulated *T*, *R*, and *A* spectra of Ag (7 nm)/TeO_2 (210 nm) for $N_p = 1$. E) Simulated *T*, *R*, and *A* spectra of Ag (7 nm)/TeO_2 (50 nm)/Ag (7 nm)/TeO_2 (50 nm) for $N_p = 2$. F) Simulated *T* spectrum as a function of θ_{inc} for mean-polarization (MT) illumination, and the $N_p = 2$.

For transparent devices, CRI is a metric that takes into account the accuracy of a color rendered under lighting conditions to that of natural light. Herein, the CRI values of Au/Ag-based ST-OPVs are around 75 (Table S2, Supporting Information), which is considerably higher in comparison with other transparent photovoltaic cells, such as hydrogenated amorphous silicon,[52] crystalline silicon,[53] dye-sensitized,[54] and perovskite solar cells.[55,56] The transmittance of ST-OPVs is mainly affected by the spectral distribution of the active layer and transparent electrode. As shown in **Figure** 2A, a transmission peak at 400–500 nm and a transmission valley at 500–700 nm occur within the visible region. The CRI value for neutral-color ST-OPVs should be as near to 100 as possible for power window applications. To achieve a uniform transmittance distribution in the visible region, FPOC as the optical modulation of ST-OPVs was designed by eliminating the transmission peak and valley. The schematic description of a FPOC's structure shows two coupled resonators in Figure 2B, where resonator 1 is the top three layers consisting of metal, lossless dielectric, and metal, and resonator 2 is layers 4–5 consisting of metal, lossless dielectric. Ag and TeO_2 are used as the metal and dielectric layer materials, respectively. The simulated transmittance spectra of Ag (7 nm)/TeO_2 (0–500 nm, $N_p = 1$) in the visible region are shown in Figure 2C. When TeO_2's thickness is below 180 nm, the derivative of Ag (7 nm)/TeO_2 has only a single transmission peak in the visible region. For example, when the thickness of TeO_2 is 50 nm (Figure S7A, Supporting Information), the wavelength of the resonant passband is about 696 nm due to the phase shift that results from reflection at the metal–dielectric interface, allowing resonance within dielectric thickness. When the TeO_2 thickness is thicker than 180 nm, the visible area exhibits two or more transmission peaks. And transmission peak with lower transmittance in the near-infrared region occurs, as shown in Figure 2D. While N_p is 2, as shown in Figure 2E, the simulated transmittance spectrum of Ag (7 nm)/TeO_2 (50 nm)/Ag (7 nm)/TeO_2 (50 nm) exhibits two adjacent transmission peaks in the visible region and high reflection from 1200 to 2500 nm, implying its excellent thermal insulation. As the modes of resonator 1 and resonator 2 are coupled, the single cavity mode was split into two distinct characteristic modes at 410 and 674 nm, respectively, corresponding to metal–dielectric resonator 1 and metal–dielectric–metal resonator 2.[57] The two resonators of FPOC share an inner Ag layer that determines their coupling strength. Due to the dispersion of the inner Ag layer, the resonant transmission peaks have different peak magnitudes. As the thickness of Ag increases (7–21 nm, Figure S7B, Supporting Information), the transmittance decreases in the whole region (400–2500 nm) and a narrower bandwidth of resonant transmission peak occurs. The thickness of the optical dielectric layers (TeO_2) in the resonant cavity also affects the position and magnitude of two resonant transmission peaks, as shown in Figure S7 (Supporting Information), implying the flexible regulation of transmittance distribution for Ag/TeO_2/Ag/TeO_2-integrated ST-OPVs. Angle dependence of transparent devices is also a crucial parameter in

real-world applications. The transmittance distributions of optimized FPOC under different incident angles are simulated, as shown in Figure 2F. The results present a nearly constant for mean-polarization incident angles from 0° to 60°. The wide angle insensitivity of FPOC is attributed to the insensible reflected phase shift, which is a mutual offset between the reflection in the cavity and the propagation caused by the incident angle change. The results indicated that FPOC with Ag/TeO_2/Ag/TeO_2 structure can be ideally integrated for ST-OPVs to achieve excellent color tunability, thermal insulation, and insensitive incident angle dependence below 60°.

To explore the influence of inner Ag's thickness for FPOC-integrated ST-OPVs, the derived devices were fabricated with an architecture of glass/ITO/PEDOT:PSS/PM6:BTP-eC9:L8-BO (75 nm)/PDINN/Au (0.8 nm)/Ag (7 nm)/TeO_2/Ag (7-21 nm)/TeO_2. To achieve a CRI close to 100, the thickness of TeO_2 layers for FPOC-integrated ST-OPVs was simulated with different inner Ag's thicknesses (11–21 nm) through Macleod film design software. The detailed simulated optical parameters are summarized in Table S3 (Supporting Information). The simulated results presented that the AVT of devices exhibited a decline from 49.12% to 39.97% along with the increasing Ag thickness (Figure S8A and Table S3, Supporting Information), while the CRI values presented a fluctuating variation at around 95. The corresponding FPOC-integrated ST-OPVs were fabricated equivalently.

The optical and photovoltaic characteristics of fabricated devices are shown in Figure S8B (Supporting Information). The experimental results show a consistent trend as the simulated ones (Figure S8C, Supporting Information). As the thickness of Ag in the resonant cavity increases, the transmittance of FPOC-integrated ST-OPV decreases in the whole visible and NIR regions, resulting in higher J_{SC}, T-SER, and NIR-SER but lower AVT (Figure S8D and Table S4, Supporting Information). Considering the photovoltaic and thermal insulation performance, LUE, T-DFE, and NIR-DFE values are proposed as the appropriate figures of merit to evaluate the neutral-color FPOC-integrated ST-OPVs. When the inner Ag is 17 nm, the highest LUE, T-DFE, and NIR-DFE values of device were obtained at 3.64%, 2.78%, and 3.30%, respectively (Table S4, Supporting Information). Furthermore, the FPOC-integrated ST-OPVs were optimized with different active layers' thicknesses where the inner Ag was set at 17 nm. An ARC (**Figure 3**A) was utilized with a configuration of (LiF/TeO_2),[4] which has been reported in our previous work.[33] The simulated optical dielectric parameters for neutral-color ST-OPVs were summarized, as listed in Table S5 and Figure S9 (Supporting Information). The thickness of the top TeO_2 layer is decreased along with the reduced thickness of the active layer. The photovoltaic performance and optical properties of the corresponding ST-OPVs were tested, as shown in Figure S10 (Supporting Information). With decreasing active layer thickness, the transmittance of derived ST-OPV increases significantly and remains uniform transmission in the visible region, resulting in improved AVT and reduced T-SER value (Table S6, Supporting Information). The CRI values of FPOC-integrated ST-OPVs are all above 96, implying the effective tunability of FPOC for neutral-color ST-OPVs. The detailed data of FPOC-integrated ST-OPVs with different active layers (65–110 nm) are summarized in Table S6 (Supporting Information). The EQE + T + R of the corresponding ST-OPVs were also measured to validate the accurate and reliable data, as shown in Figure S11 (Supporting Information), and all the values are below 100%.

To intuitively reveal the effect of FPOC on ST-OPVs, the photovoltaic performance of 75 nm devices without and with FPOC were listed in Figure 3B. The 75 nm FPOC-integrated ST-OPV exhibited the highest LUE of 3.90% with a decent PCE of 9.03%, a high AVT of 43.15%, and a CRI of 97.31 with a CIELAB coordinate (L^*, a^*, b^*, Supporting Information) of (71.7, −2.45, 0.48). Compared to the Au/Ag-based counterpart, FPOC-integrated ST-OPV (75 nm) showed a comprehensive performance enhancement except for the slightly decreasing PCE, which is attributed to the decreasing J_{SC}. The EQE results indicated that FPOC-integrated ST-OPV shows a decreased EQE response in the visible region, while an increased response in the near-infrared region, compared to the Au/Ag-based counterpart (Figure 3C). The variation tendency of J_{SC} is further verified through the simulation of the exciton generation rate for ST-OPVs with and without FPOC (Figure 3D). The integration of FPOC can effectively eliminate the peaks and valleys of the transmittance spectra, resulting in a uniform distribution in the visible region (Figure 3E and Figure S10C (Supporting Information)). Compared to the Au/Ag-based counterpart, the CIE 1931 coordinates of FPOC-integrated ST-OPVs are closer to that of AM1.5G (Figure 3F and Figure S10D (Supporting Information)). The FPOC-integrated ST-OPVs exhibited a higher NIR solar energy rejection than the Au/Ag-based counterpart due to the enhanced reflection (Figure 3G and Figure S12 (Supporting Information)). The T-SER and NIR-SER values of 75 nm FPOC-integrated ST-OPV are 75.00% and 89.11%, respectively, corresponding to T-DFE of up to 2.92% and NIR-DFE of 3.47%. An enhancement of over 20% in NIR-DFE was achieved compared to that of Au/Ag-based counterpart (**Table 1**), implying its superior thermal insulation of FPOC-integrated ST-OPVs. Besides, the 65 nm FPOC-integrated ST-OPV exhibited the highest CRI of 99.23% with a CIELAB coordinate of (72.9, −0.28, −0.08), which is the best result for semi-transparent devices reported in the literature to date (Figure 3H and Table S7 (Supporting Information)). The T-SER and NIR-SER values of 65 nm FPOC-integrated ST-OPV are maintained at 73.86% and 88.68%, respectively, which is mainly determined by the optical properties of FPOC. To reveal the difference in human color perception for AM1.5G, Au/Ag-based ST-OPV (75 nm), and FPOC-integrated ones (75 and 65 nm), the CIELAB color spaces were depicted in Figure S13 (Supporting Information). As shown in Figure 3I, scaled-up ST-OPVs (20 mm × 20 mm) with and without FPOC were also fabricated to explore the visibility and color-rendering capacity. Visually, the FPOC-integrated ST-OPVs can rival the quality of glass as windows, where colorful balls serve as the background. The 100 mm^2 FPOC-integrated ST-OPV exhibited an inferior PCE of 8.46% owing to the increased sheet resistance (Figure S14, Supporting Information). The results demonstrate the flexibility of Ag/TeO_2/Ag/TeO_2-based FPOC for neutral-color ST-OPVs with CRI approaching 100. Meanwhile, the photovoltaic performance (LUE and AVT) and thermal insulation properties (T-SER and NIR-SER) of ST-OPVs can be simultaneously improved by integrating FPOC.

Device stability was conducted for ST-OPVs with and without FPOC according to the International Summit on Organic

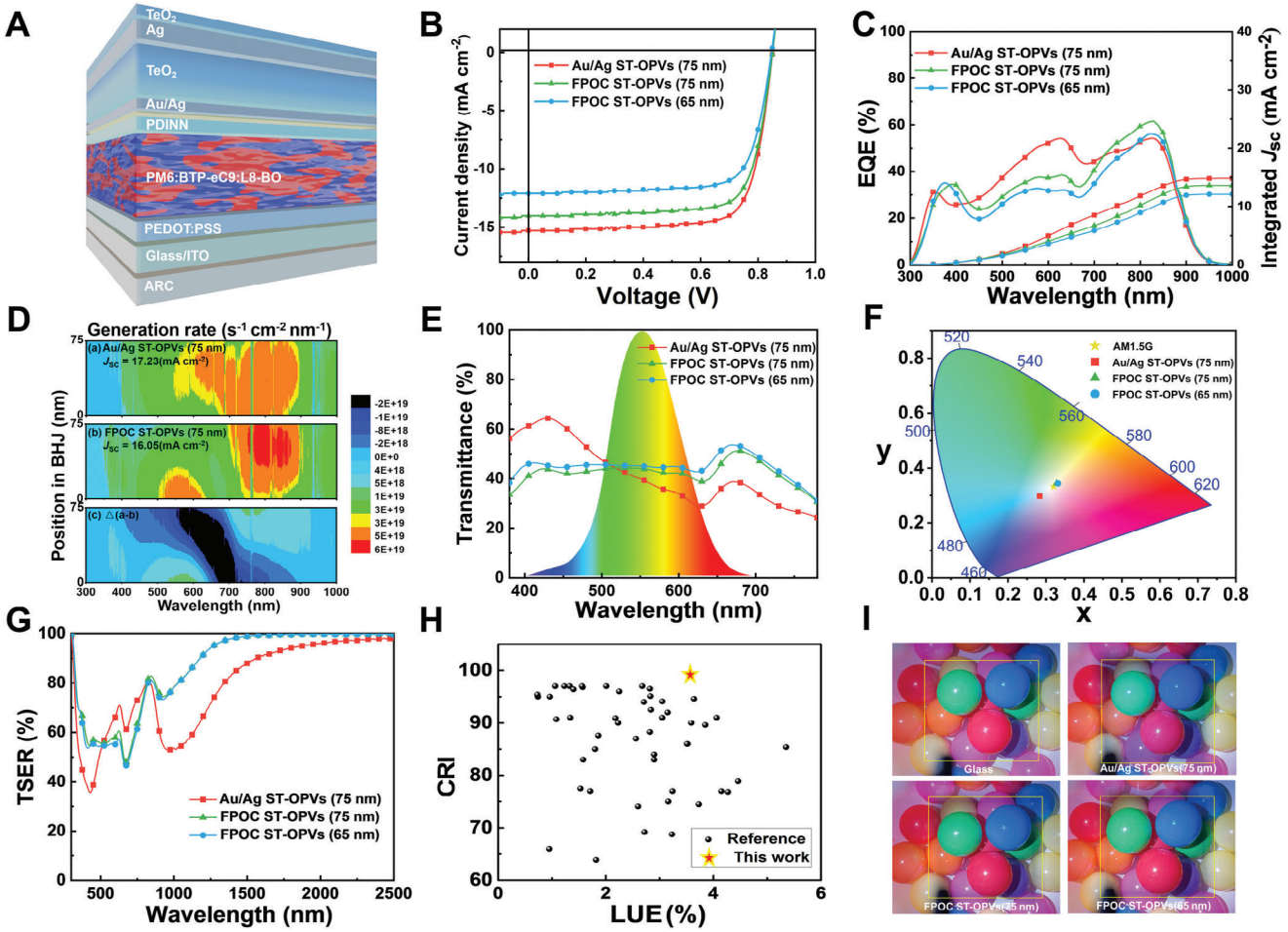

Figure 3. Photovoltaic performance and optical properties of Au/Ag-based ST-OPV (75 nm) and FPOC-integrated ST-OPV s (75 and 65 nm). A) The FPOC-integrated ST-OPV with the architecture of ARC/glass/ITO/PEDOT:PSS/PM6:BTP-eC9:L8-BO/PDINN/Au/Ag/TeO_2/Ag/TeO_2. B) *J–V* curves. C) EQE curves. D) Simulation of the exciton generation in ST-OPVs with and without FPOC. E) Experimental transmittance spectra (380–780 nm). F) CIE 1931 coordinates. G) T-SER spectra (300–2500 nm). H) Summary of the reported LUE and CRI of ST-OPVs. I) Photograph of glass, Au/Ag-based ST-OPV (75 nm) and FPOC-integrated ST-OPVs (75 and 65 nm) using colorful balls as background.

PV stability-light-soaking (ISOS-L-1) protocols.[58] Continuous light-emitting diode (LED) light with a light intensity of 274 600 lux was used as a stable light source and equivalent to AM1.5G illumination (Figure S15, Supporting Information). The degradation of ST-OPVs is rapid under the ISOS-L-1 protocol, which could be owing to the intrinsically unstable morphology of organic active layer under illumination. FPOC-integrated and Au/Ag-based ST-OPVs remained at 55% and 30% of their initial PCE after 400 h illumination, respectively. The results indicated the effective protection of FPOC as a buffer layer in the encapsulation for ST-OPVs.

To intuitively investigate their thermal insulation performance, an actual scene was set up that a black object was illuminated through air, glass, Au/Ag-based ST-OPV, and FPOC-integrated ST-OPV as a window, respectively (**Figure 4**). The temperature changes of the windows and black objects were recorded by an IR camera. After 5 min xenon lamp illumination, the ambient temperature was 66.29 °F (Figure 4B), and the temperature of the black object reached 105.02, 96.55, 88.03, and 84.82 °F through air, glass, Au/Ag-based ST-OPV, and FPOC-integrated ST-OPV as a window, respectively. NIR light can produce more heat than visible light because the longer wavelength of NIR light

Table 1. The photovoltaic and optical performance of the Au/Ag-based ST-OPV (75 nm) and FPOC-integrated ST-OPVs (75 and 65 nm).

Devices	PCE [%]	AVT [%]	LUE [%]	1931 CIE	CIELAB	CRI	T-SER [%]	NIR-SER [%]	T-DFE [%]	NIR-DFE [%]
Au/Ag ST-OPV (75 nm)	9.81	38.91	3.82	(0.2836, 0.2975)	(68.9, −1.6, −20.99)	81.21	67.29	75.67	2.57	2.89
FPOC ST-OPV (75 nm)	9.03	43.15	3.90	(0.3289, 0.3472)	(71.7, −2.45, 0.48)	97.31	75.00	89.11	2.92	3.47
FPOC ST-OPV (65 nm)	7.88	45.08	3.55	(0.3315, 0.3439)	(72.9, −0.28, −0.08)	99.23	73.86	88.68	2.62	3.15

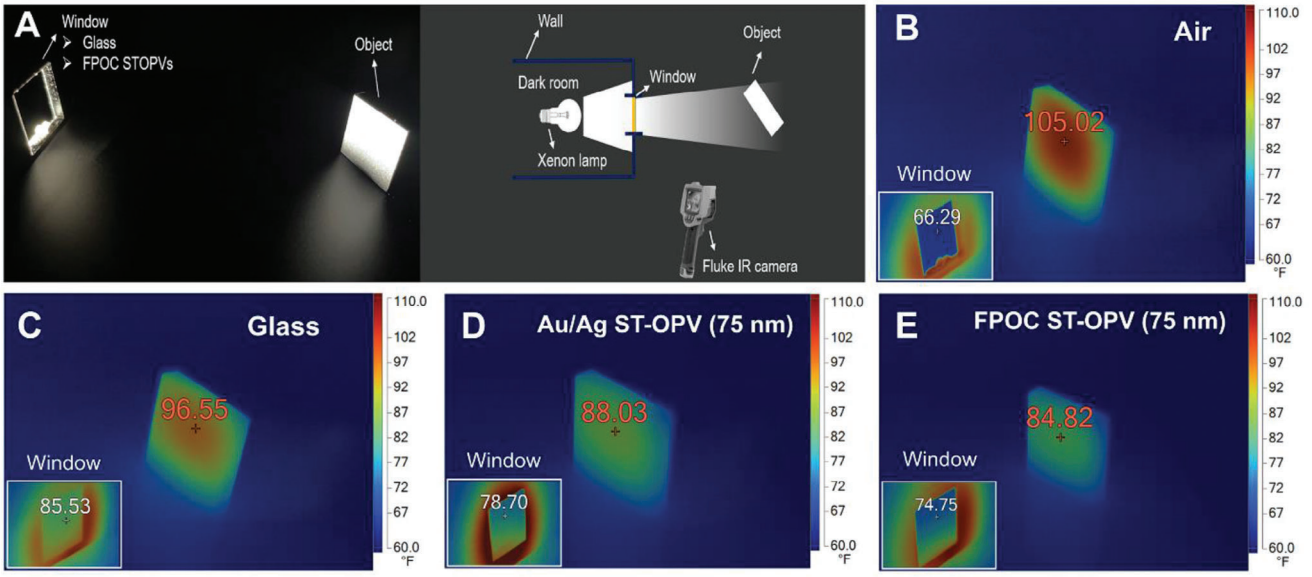

Figure 4. Thermal images captured by a Fluke IR camera for measuring the thermal rejection. A) The experimental testing setup for thermal rejection performance is presented in the physical diagram (left) and the schematic diagram (right). Thermal image of the black object and the windows after 5 min exposure under the xenon lamp using (B) air, C) glass, D) Au/Ag-based ST-OPV, and E) FPOC-integrated ST-OPVs as the windows.

with lower frequency allows it to interact more strongly with molecules and penetrate deeper, causing them to vibrate and generate heat. FPOC-integrated ST-OPV has the highest NIR-SER of 89.11% in these windows, resulting in the lowest temperature of the black object after 5 min xenon lamp illumination. Similarly, the temperature of FPOC-integrated ST-OPV (74.75 °F) is also lower than that of glass (85.53 °F) or Au/Ag-based ST-OPV (78.70 °F) owing to the higher NIR-SER of FPOC-integrated ST-OPV. By adopting Wheeler's estimation,[59] considering the photovoltaic performance of 9% PCE and thermal insulation, we estimated that the FPOC-integrated ST-OPV can reach about 40% energy use reduction. These experimental results demonstrate

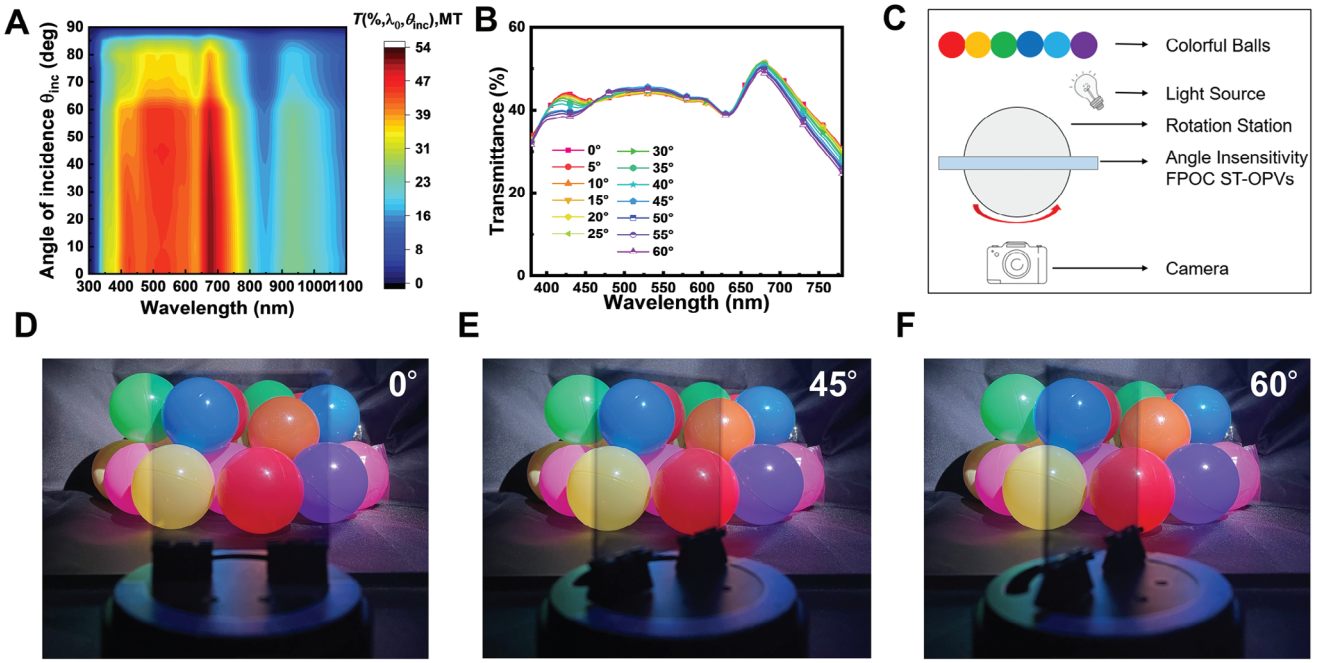

Figure 5. The transmittance spectra, experimental setup, and observations of the incident angle insensitivity FPOC ST-OPVs (75 nm) device. A) The simulated transmittance spectra for mean-polarized light. B) The experimental transmittance spectra for mean-polarized light. C) Schematic of the experiment setup. D) θ_{inc} is 0°. E) θ_{inc} is 45°. F) θ_{inc} is 60°.

that FPOC-integrated ST-OPV can significantly reduce the solar heat flux and has great potential to be applied as a window for power generation and thermal insulation in BIPVs or car windows, providing new ideas for future energy harvesting methods.

To investigate the angle sensitivity of FPOC-integrated ST-OPVs, the mean-polarization transmittance spectra of the FPOC-integrated ST-OPVs at different incidence angles θ_{inc} are shown in **Figure** 5A. The transmission spectrum should be almost unchanged theoretically if the cumulative propagation phase shift through the proposed structure remains constant as the angle of incidence varies. As a result, FPOC-integrated ST-OPVs exhibit excellent angle independence up to ±60° (Figure 5B and Figure S16 (Supporting Information)). More specifically, when the angle of incident light varies from 0° to 60°, the CIE color spaces of devices were located between (0.3287, 0.3467) and (0.3307, 0.3542), indicating that the position is nearly constant. The AVT and CRI values of devices under different angles of incident light are kept around 43% and 97, respectively (Table S8, Supporting Information). To demonstrate the angle-insensitive optical characteristics of FPOC-integrated ST-OPVs, it is placed in front of colorful toy balls, as shown in Figure 5C. The FPOC-integrated ST-OPVs appear highly transparent and neutral color when θ_{inc} is from 0° to 60° (Figure 5D–F). The outstanding angle insensitivity (±60°) of FPOC-integrated ST-OPVs greatly accelerates its commercialization for BIPVs.

3. Conclusion

In conclusion, a novel visible dual-band-pass FPOC of Ag (7 nm)/TeO_2/Ag (17 nm)/TeO_2 with excellent neutral-color tunability and thermal insulation was designed for ST-OPVs. The champion 65 nm FPOC-integrated ST-OPVs demonstrate the highest CRI of 99.23 with a CIELAB coordinate of (72.9, −0.28, −0.08), which is the highest reported value for ST-OPVs in the literature. The 75 nm FPOC-integrated ST-OPV achieves excellent overall performance—a champion LUE of 3.90% with an AVT of 43.15%, a high CRI of 97.31, and an excellent NIR-SER of about 90% simultaneously. Due to the flexibility of Ag/TeO_2/Ag/TeO_2-based FPOC, all of the ST-OPVs with different active layer thicknesses can realize near-ideal neutral color, where the CIE 1931 color coordinates are close to AM1.5G. Besides, FPOC-integrated ST-OPVs exhibit superior thermal insulation properties, where the highest T-DFE and NIR-DFE values of 2.92% and 3.47% were obtained. Meanwhile, FPOC-integrated ST-OPVs possess adequate angular insensitivity up to ±60° and still maintain a neutral color. Our results demonstrate the flexibility and multifunctionality of Ag/TeO_2/Ag/TeO_2-based FPOC for constructing neutral-color, heat-insulated, and angular-insensitive ST-OPVs with high performance, thereby significantly promoting its future commercial applications.

Supporting Information

Supporting Information is available from the Wiley Online Library or from the author.

Acknowledgements

The authors acknowledge the support from the Research Grants Council of Hong Kong (Project Nos. 15221320, 15307922, C5037-18G, C4005-22Y), the RGC Senior Research Fellowship Scheme (Grant No. SRFS2223-5S01), the Hong Kong Polytechnic University: Sir Sze-yuen Chung Endowed Professorship Fund (Grant No. 8-8480), the RISE (Grant No. Q-CDBK), the PRI (Grant Nos. 1-CD7X, G-SAC5), and the Hong Kong Scholar Program.

Conflict of Interest

The authors declare no conflict of interest.

Data Availability Statement

The data that support the findings of this study are available from the corresponding author upon reasonable request.

Keywords

angular insensitivity, color rendering index, neutral color, semitransparent organic photovoltaics, thermal insulation

Received: April 10, 2024
Revised: June 21, 2024
Published online: July 18, 2024

[1] P. Cheng, G. Li, X. Zhan, Y. Yang, *Nat. Photonics* **2018**, *12*, 131.
[2] J. Hou, O. Inganäs, R. H. Friend, F. Gao, *Nat. Mater.* **2018**, *17*, 119.
[3] Y. Li, G. Xu, C. Cui, Y. Li, *Adv. Energy Mater.* **2018**, *8*, 1701791.
[4] H. Shi, R. Xia, G. Zhang, H.-L. Yip, Y. Cao, *Adv. Energy Mater.* **2019**, *9*, 1803438.
[5] G. Li, V. Shrotriya, J. Huang, Y. Yao, T. Moriarty, K. Emery, Y. Yang, *Nat. Mater.* **2005**, *4*, 864.
[6] G. Li, W.-H. Chang, Y. Yang, *Nat. Rev. Mater.* **2017**, *2*, 17043.
[7] P. Bi, S. Zhang, Z. Chen, Y. Xu, Y. Cui, T. Zhang, J. Ren, J. Qin, L. Hong, X. Hao, J. Hou, *Joule* **2021**, *5*, 2408.
[8] J. Fu, P. W. K. Fong, H. Liu, C.-S. Huang, X. Lu, S. Lu, M. Abdelsamie, T. Kodalle, C. M. Sutter-Fella, Y. Yang, G. Li, *Nat. Commun.* **2023**, *14*, 1760.
[9] Y. Zhang, W. Deng, C. E. Petoukhoff, X. Xia, Y. Lang, H. Xia, H. Tang, H. T. Chandran, S. Mahadevan, K. Liu, P. W. K. Fong, Y. Luo, J. Wu, S.-W. Tsang, F. Laquai, H. Wu, X. Lu, Y. Yang, G. Li, *Joule* **2024**, *8*, 509.
[10] L. Wang, C. Chen, Y. Fu, C. Guo, D. Li, J. Cheng, W. Sun, Z. Gan, Y. Sun, B. Zhou, C. Liu, D. Liu, W. Li, T. Wang, *Nat. Energy* **2024**, *9*, 208.
[11] Z. Zheng, J. Wang, P. Bi, J. Ren, Y. Wang, Y. Yang, X. Liu, S. Zhang, J. Hou, *Joule* **2022**, *6*, 171.
[12] J. Yi, G. Zhang, H. Yu, H. Yan, *Nat. Rev. Mater.* **2024**, *9*, 46.
[13] C. Yan, S. Barlow, Z. Wang, H. Yan, A. K. Y. Jen, S. R. Marder, X. Zhan, *Nat. Rev. Mater.* **2018**, *3*, 18003.
[14] Y. Cui, Y. Xu, H. Yao, P. Bi, L. Hong, J. Zhang, Y. Zu, T. Zhang, J. Qin, J. Ren, Z. Chen, C. He, X. Hao, Z. Wei, J. Hou, *Adv. Mater.* **2021**, *33*, 2102420.
[15] J. Fu, Q. Yang, P. Huang, S. Chung, K. Cho, Z. Kan, H. Liu, X. Lu, Y. Lang, H. Lai, F. He, P. W. K. Fong, S. Lu, Y. Yang, Z. Xiao, G. Li, *Nat. Commun.* **2024**, *15*, 1830.
[16] C. He, Y. Pan, Y. Ouyang, Q. Shen, Y. Gao, K. Yan, J. Fang, Y. Chen, C.-Q. Ma, J. Min, C. Zhang, L. Zuo, H. Chen, *Energy Environ. Sci.* **2022**, *15*, 2537.
[17] K. Forberich, F. Guo, C. Bronnbauer, C. J. Brabec, *Energy Technol.* **2015**, *3*, 1051.
[18] C. Ballif, L.-E. Perret-Aebi, S. Lufkin, E. Rey, *Nat. Energy* **2018**, *3*, 438.
[19] C. Sun, R. Xia, H. Shi, H. Yao, X. Liu, J. Hou, F. Huang, H.-L. Yip, Y. Cao, *Joule* **2018**, *2*, 1816.

[20] N. Zhang, T. Jiang, C. Guo, L. Qiao, Q. Ji, L. Yin, L. Yu, P. Murto, X. Xu, *Nano Energy* **2020**, *77*, 105111.
[21] D. Wang, H. Liu, Y. Li, G. Zhou, L. Zhan, H. Zhu, X. Lu, H. Chen, C.-Z. Li, *Joule* **2021**, *5*, 945.
[22] S.-Y. Chang, P. Cheng, G. Li, Y. Yang, *Joule* **2018**, *2*, 1039.
[23] T. Jiang, G. Zhang, R. Xia, J. Huang, X. Li, M. Wang, H. L. Yip, Y. Cao, *Mater. Today Energy* **2021**, *21*, 100807.
[24] P. Cheng, H.-C. Wang, Y. Zhu, R. Zheng, T. Li, C.-H. Chen, T. Huang, Y. Zhao, R. Wang, D. Meng, Y. Li, C. Zhu, K.-H. Wei, X. Zhan, Y. Yang, *Adv. Mater.* **2020**, *32*, 2003891.
[25] N. Liang, R. Tian, Y. Xu, H. Yao, H. Yang, Y. Wei, X. Xin, R. Chen, T. Zhai, Z. Wang, J. Hou, *Adv. Mater.* **2023**, *35*, 2300360.
[26] H.-C. Wang, P. Cheng, S. Tan, C.-H. Chen, B. Chang, C.-S. Tsao, L.-Y. Chen, C.-A. Hsieh, Y.-C. Lin, H.-W. Cheng, Y. Yang, K.-H. Wei, *Adv. Energy Mater.* **2021**, *11*, 2003576.
[27] J. Jing, S. Dong, K. Zhang, Z. Zhou, Q. Xue, Y. Song, Z. Du, M. Ren, F. Huang, *Adv. Energy Mater.* **2022**, *12*, 2200453.
[28] Z. Hu, Z. Wang, Q. An, F. Zhang, *Sci. Bull.* **2020**, *65*, 131.
[29] P. Yin, Z. Yin, Y. Ma, Q. Zheng, *Energy Environ. Sci.* **2020**, *13*, 5177.
[30] Y. Li, C. He, L. Zuo, F. Zhao, L. Zhan, X. Li, R. Xia, H.-L. Yip, C.-Z. Li, X. Liu, H. Chen, *Adv. Energy Mater.* **2021**, *11*, 2003408.
[31] X. Liu, Y. Zhao, J. Yu, R. Zhu, *Mater. Chem. Front.* **2021**, *5*, 8197.
[32] I. Burgués-Ceballos, L. Lucera, P. Tiwana, K. Ocytko, L. W. Tan, S. Kowalski, J. Snow, A. Pron, H. Bürckstümmer, N. Blouin, G. Morse, *Joule* **2021**, *5*, 2261.
[33] X. Liu, Z. Zhong, R. Zhu, J. Yu, G. Li, *Joule* **2022**, *6*, 1918.
[34] S. Guan, Y. Li, K. Yan, W. Fu, L. Zuo, H. Chen, *Adv. Mater.* **2022**, *34*, 2205844.
[35] Y. Li, X. Guo, Z. Peng, B. Qu, H. Yan, H. Ade, M. Zhang, S. R. Forrest, *Proc. Natl. Acad. Sci. USA* **2020**, *117*, 21147.
[36] C. J. Traverse, R. Pandey, M. C. Barr, R. R. Lunt, *Nat. Energy* **2017**, *2*, 849.
[37] Y. Li, C. Ji, Y. Qu, X. Huang, S. Hou, C.-Z. Li, L.-S. Liao, L. J. Guo, S. R. Forrest, *Adv. Mater.* **2019**, *31*, 1903173.
[38] Q. Xue, R. Xia, C. J. Brabec, H.-L. Yip, *Energy Environ. Sci.* **2018**, *11*, 1688.
[39] W. Yang, W. Wang, Y. Wang, R. Sun, J. Guo, H. Li, M. Shi, J. Guo, Y. Wu, T. Wang, G. Lu, C. J. Brabec, Y. Li, J. Min, *Joule* **2021**, *5*, 1209.
[40] K.-S. Chen, J.-F. Salinas, H.-L. Yip, L. Huo, J. Hou, A. K. Y. Jen, *Energy Environ. Sci.* **2012**, *5*, 9551.
[41] W. Yu, X. Jia, Y. Long, L. Shen, Y. Liu, W. Guo, S. Ruan, *ACS Appl. Mater. Interfaces* **2015**, *7*, 9920.
[42] P. Shen, G. Wang, B. Kang, W. Guo, L. Shen, *ACS Appl. Mater. Interfaces* **2018**, *10*, 6513.
[43] X. Yuan, R. Sun, Y. Wu, T. Wang, Y. Wang, W. Wang, Y. Yu, J. Guo, Q. Wu, J. Min, *Adv. Funct. Mater.* **2022**, *32*, 2200107.
[44] M. R. Gadsdon, J. Parsons, J. R. Sambles, *J. Opt. Soc. Am. B* **2009**, *26*, 734.
[45] S. Kim, M. Man, M. Qi, K. J. Webb, *Opt. Lett.* **2014**, *39*, 5784.
[46] M. Scalora, M. J. Bloemer, A. S. Pethel, J. P. Dowling, C. M. Bowden, A. S. Manka, *J. Appl. Phys.* **1998**, *83*, 2377.
[47] Y. Bai, F. Han, R. Shi, F. Wang, S. Jiang, J. Wang, Z. Tan, *Sol. RRL* **2022**, *6*, 2200174.
[48] B. N. Liang, R. Tian, Y. Xu, H. Yao, H. Yang, Y. Wei, X. Xin, R. Chen, T. Zhai, Z. Wang, J. Hou, *Adv. Mater.* **2023**, *35*, 2300360.
[49] D. Wang, R. Qin, G. Zhou, X. Li, R. Xia, Y. Li, L. Zhan, H. Zhu, X. Lu, H. L. Yip, H. Chen, C. Z. Li, *Adv. Mater.* **2020**, *32*, 2001621.
[50] H. Kim, H.-S. Kim, J. Ha, N.-G. Park, S. Yoo, *Adv. Energy Mater.* **2016**, *6*, 1502466.
[51] X. Li, R. Xia, K. Yan, H.-L. Yip, H. Chen, C.-Z. Li, *Chin. Chem. Lett.* **2020**, *31*, 1608.
[52] J.-S. Cho, Y. H. Seo, B.-H. Choi, A. Cho, A. Lee, M. J. Shin, K. Kim, S. K. Ahn, J. H. Park, J. Yoo, D. Shin, I. Jeong, J. Gwak, *Sol. Energy Mater. Sol. Cells* **2019**, *202*, 110078.
[53] J. Peng, D. C. Curcija, A. Thanachareonkit, E. S. Lee, H. Goudey, S. E. Selkowitz, *Appl. Energy* **2019**, *242*, 854.
[54] K. Kim, S. K. Nam, J. H. Moon, *Chin. Chem. Lett.* **2020**, *3*, 5277.
[55] J. Lee, B. Shin, S. Kim, S. H. Cho, Y. Jung, K.-T. Park, C. Son, Y. H. Chu, D. G. Ryu, S. Yoon, M. Choi, H.-Y. Kim, Y. S. Lee, *ACS Appl. Mater. Interfaces* **2021**, *13*, 58475.
[56] S.-H. Lim, H.-J. Seok, D.-H. Choi, S.-K. Kim, D.-H. Kim, H.-K. Kim, *ACS Appl. Mater. Interfaces* **2021**, *13*, 27353.
[57] Q. Li, T. Wang, Y. Su, M. Yan, M. Qiu, *Opt. Express* **2010**, *18*, 8367.
[58] M. O. Reese, S. A. Gevorgyan, M. Jørgensen, E. Bundgaard, S. R. Kurtz, D. S. Ginley, D. C. Olson, M. T. Lloyd, P. Morvillo, E. A. Katz, A. Elschner, O. Haillant, T. R. Currier, V. Shrotriya, M. Hermenau, M. Riede, K. R. Kirov, G. Trimmel, T. Rath, O. Inganäs, F. Zhang, M. Andersson, K. Tvingstedt, M. Lira-Cantu, D. Laird, C. McGuiness, S. Gowrisanker, M. Pannone, M. Xiao, J. Hauch, et al., *Sol. Energy Mater. Sol. Cells* **2011**, *95*, 1253.
[59] V. M. Wheeler, J. Kim, T. Daligault, B. A. Rosales, C. Engtrakul, R. C. Tenent, L. M. Wheeler, *One Earth* **2022**, *5*, 1271.